The impact of ENSO on Southern African rainfall in CMIP5 ocean atmosphere coupled climate models

Dieppois, B. , Rouault, M. and New, M.

Climate Dynamics

The impact of El Niño on Southern African rainfall in CMIP5 Ocean Atmosphere coupled climate models

--Manuscript Draft--

Manuscript Number:	
Full Title:	The impact of El Niño on Southern African rainfall in CMIP5 Ocean Atmosphere coupled climate models
Article Type:	Original Article
Keywords:	Southern Africa; rainfall; El Niño Southern Oscillation (ENSO); coupled model; CMIP5; teleconnection
Corresponding Author:	Bastien Dieppois African Climate & Develpment Intitiative, University of Cape Town Cape Town, Western Cape SOUTH AFRICA
Corresponding Author Secondary Information:	
Corresponding Author's Institution:	African Climate & Develpment Intitiative, University of Cape Town
Corresponding Author's Secondary Institution:	
First Author:	Bastien Dieppois
First Author Secondary Information:	
Order of Authors:	Bastien Dieppois
	Mathieu Rouault
	Mark New
Order of Authors Secondary Information:	
Abstract:	We study the ability of 24 Ocean Atmosphere global coupled models from the Coupled Model Intercomparison Project 5 (CMIP5) to reproduce the teleconnections between El Niño Southern Oscillation (ENSO) and Southern African rainfall in austral summer using historical forced simulations, with a focus on El Niño. Overestimations of summer rainfall occur over Southern Africa in all CMIP5 models. Abnormal westward extensions of ENSO patterns are a common feature of all CMIP5 models while the warming of Indian Ocean that happens during ENSO are not correctly reproduced. This could impact the teleconnection between ENSO and Southern African rainfall which is represented with mixed success in CMIP5 models. From the near-surface to mid-troposphere, CMIP5 models underestimate the observed anomalous pattern of pressure occurring over Southern Africa that leads to dry conditions during El Niño years. Large-scale anomalies of suppressed deep-convection over the tropical maritime continent and enhanced convection from the central to eastern Pacific are correctly simulated. However, regional biases occur above Africa and the Indian Ocean, particularly in the position of the South Indian Convergence Zone (SICZ) during El Niño, which can lead to the wrong sign in rainfall anomalies in the northwest part of South Africa.
Suggested Reviewers:	Damian Maurice Lawler, Professor CAWR, Coventry University Damian.Lawler@coventry.ac.uk
	Yves Richard, Professor CRC, Burgundy University Yves.Richard@u-bourgogne.fr One of the most famous expert in South African climate
	Nathalie Phillipon, Dr CNRS researcher, CRC, Burgundy University Nathalie.Philippon@u-bourgogne.fr

	Bruce Hewitson, Professor CSAG, University of Cape Town hewitson@csag.uct.ac.za One of the most famous expert in African climate, and CMIP5 experiments.

The impact of El Niño on Southern African rainfall in CMIP5 Ocean Atmosphere coupled climate models

Bastien Dieppois [1, 2], Mathieu Rouault [2,3], Mark New [1]
bastien.dieppois@univ-rouen.fr

[1] African Climate & Development Initiative, University of Cape Town, RSA
[2] Department of Oceanography, MARE Institute, University of Cape Town, RSA
3 Nansen-Tutu Center for Marine Environmental Research, University of Cape Town, RSA

Abstract We study the ability of 24 Ocean Atmosphere global coupled models from the Coupled Model Intercomparison Project 5 (CMIP5) to reproduce the teleconnections between El Niño Southern Oscillation (ENSO) and Southern African rainfall in austral summer using historical forced simulations, with a focus on El Niño. Overestimations of summer rainfall occur over Southern Africa in all CMIP5 models. Abnormal westward extensions of ENSO patterns are a common feature of all CMIP5 models while the warming of Indian Ocean that happens during ENSO are not correctly reproduced. This could impact the teleconnection between ENSO and Southern African rainfall which is represented with mixed success in CMIP5 models. From the near-surface to mid-troposphere, CMIP5 models underestimate the observed anomalous pattern of pressure occurring over Southern Africa that leads to dry conditions during El Niño years. Large-scale anomalies of suppressed deep-convection over the tropical maritime continent and enhanced convection from the central to eastern Pacific are correctly simulated. However, regional biases occur above Africa and the Indian Ocean, particularly in the position of the South Indian Convergence Zone (SICZ) during El Niño, which can lead to the wrong sign in rainfall anomalies in the northwest part of South Africa.

Keywords Southern Africa, rainfall, El Niño Southern Oscillation (ENSO), coupled model, CMIP5, teleconnection

1. Introduction

The El Niño Southern Oscillation (ENSO) can be considered as the leading global climate mode of variability driving interannual rainfall variability in Southern Africa. El Niño events favor droughts in this region (Ropelewski and Halpert 1987 1989; Lindesay 1988; Mason and Jury 1997; Rouault and Richard 2005), especially since the late 1970s (Richard et al. 2000, 2001; Phillipon et al. 2012). Recent studies have shown that ENSO effects on South African rainfall respond to interactions between the interannual and synoptic timescales (Pohl et al. 2009; Fauchereau et al. 2009). Cook (2001) proposed that ENSO generates atmospheric Rossby waves in the southern hemisphere which could be responsible for an eastward shift of the South Indian Convergence Zone (SICZ), where most of the synoptic-scale bearing systems that affect Southern Africa preferably develop (Todd and Washington, 1999; Todd et al. 2004, Hart et al. 2012a, b). Another hypothesis suggested by Nicholson (1997) and Nicholson and Kim (1997) is that Indian Ocean SST anomalies could shift atmospheric convection and rainfall eastward during El Niño events. A positive pressure anomaly above the continent during El Niño (Mulenga *et al*, 2003) could also affect the diurnal cycle of rainfall in Southern Africa (Rouault et al. 2013).

Although a number of previous studies have attempted to systematically evaluate the performance of coupled models to simulate the teleconnections between ENSO and tropical rainfall (Joly et al. 2007; Yang and DelSole 2012; Langenbrunner and Neelin 2013; Rowell 2013), little has been done to assess the capacity of such models to reproduce the teleconnections between El Niño Southern Oscillation (ENSO) and Southern African rainfall. In this study, we examine the ability of atmosphere-ocean global coupled climate models (AOGCMs) to reproduce observed teleconnections between ENSO and Southern African rainfall with a focus on El Niño using historical runs of the Coupled Model Intercomparison

Project 5 (CMIP5). In Section 2, we discuss data, after which we evaluate the ability of coupled models to simulate mean rainfall in Southern Africa and ENSO pattern in the Pacific. Analysis of austral summer El Niño-rainfall teleconnections with a focus on Southern Africa is presented in Section 4. The atmospheric dynamics during El Niño are presented in Section 5 and the impact of ENSO on adjacent ocean is presented in Section 6.

2. Data

2.1. Observations

The Climatic Research Unit (CRU) dataset is used to compare observed and simulated Southern African rainfall. The CRU TS 3.21 rainfall field is produced on a 0.5°×0.5° grid and is derived from monthly rainfall provided by about 4000 weather stations distributed around the world over the last century (Harris et al. 2014; see also badc.nerc.ac.uk/view/badc.nerc.ac.uk for more explanations on the CRU TS 3.21). We use monthly SST data from the extended reconstructed sea-surface temperature (ERSST) of the National Climatic Data Centre. The ERSST gridded data are generated using in situ data from the Comprehensive Ocean-Atmosphere Data Set and improved statistical methods allowing stage reconstruction using sparse data over a 2.5°×2.5° resolution grid. The ERSST.v3b version is an improved extended reconstruction and which does not use satellite data (Smith et al. 2008). NCEP/NCAR-1 (NCEP-1) reanalyses are used to infer monthly atmospheric dynamics (Kalnay et al. 1996). Five parameters – meridional (V) and zonal (U) wind, sea-level pressure (SLP), geopotentiel height at 500 hPa (z500) and calculated outgoing longwave radiation (OLR) are considered here. Note that Camberlin et al. (2001) detected an abrupt shift in NCEP-1 geopotential height and zonal wind over large parts of tropical Africa around 1967/68. This artefact may be due to changes in techniques and data used for assimilation.

2.2. CMIP5 Model output

We use 24 individual AOGCMs with a focus on austral summer – December, January and February (DJF) – the core of the Southern African rainy season (Table 1). Data between 1950 and 2005 are sourced from the Coupled Model Intercomparison Project (CMIP) using the "historical" experiment from the CMIP phase 5 (CMIP5) database (Taylor et al. 2012). These experiments simulate climate variability and trends from the mid-19th century to the late 20th or early 21st century and are driven by realistic anthropogenic and natural forcing's (*e.g.* solar, volcanic, sulphate aerosol and greenhouse gas, land use). The initialization schemes are model dependent. For instance, MIROC 5 uses an ocean only initialization schemes (Tatebe et al. 2012), while CCSM4 uses ocean and ice initial conditions from an historical experiment (Yeager et al. 2012). The spatial resolution of the various models ranges from 1.125° to 4.5° for the atmosphere component, and from 0.23° to 4.5° for the ocean component. Where an ensemble of simulations for an individual model is available (Table 1), all calculations are performed on each member before showing the overall result as an ensemble average. Finally, a multimodel mean is computed to summarize the results.

3. South African rainfall and ENSO variability: CMIP5 vs. Observations

3.1. South African rainfall

A monthly rainfall index is calculated over 34°–20°S and 10°–36°E between 1950 and 2005 (using land points only for the CMIP5 models). Figure 1a shows the annual cycle of South African rainfall in models and in observations. The models capture correctly the timing of the annual cycle of rainfall but overestimate the annual cycle by 10 to 20 mm per month. By comparing the coefficient of variations, *i.e.* the ratio of the standard deviation to the mean, we examined the performance of the CMIP5 models to reproduce the temporal variance of observed DJF rainfall (Fig. 1b). The amplitude of interannual DJF rainfall variability is lower in all CMIP5 models than in the observations (Fig. 1b).

The spatial coherency of DJF South African rainfall spatial mean patterns is then investigated using a Taylor diagram (Fig. 1c), which provides a way of graphically summarizing how closely a set of spatial mean patterns match observations. The similarity is quantified in terms of their correlation, their centered root-mean-square difference (RMS) and the amplitude of their variations (represented by their standard deviation [SD]). A reference dataset (observational data; blue square) is plotted along the x-axis. The correlation between model outputs and observation represented by azimuthal angle (dashed lines), and the radial distance (blue dashed circles) from the origin represents the SD (blue circles; Fig. 1c). The distance between each CMIP5 models and observation is proportional to the RMS error after removal of the average (green dashed circles). The spatial mean patterns from CMIP5 experiments are correctly represented, as the spatial correlation between model outputs and observed rainfall is always higher than 0.65, and can reach more than 0.9. The biases related to RMS difference between the simulated and observed spatial mean patterns, which is proportional to the distance to the blue square on the x-axis, are between 0.3 and 1.35 mm per month. The spatial variability (SD) of some CMIP5 models is similar to observation (blue circle), while other models show greater or weaker variations than the observation pattern.

Figure 2 shows the DJF differences between simulations and observation. As illustrated by the multimodel mean, most of the individual CMIP5 models significantly overestimate DJF rainfall. These overestimations are distributed along a NW-SE direction. Maximal differences are identified over the southeastern coastal regions of Southern Africa, Botswana and Namibia. Meanwhile, some models display a significant underestimation over the northwesternmost regions. It is particularly the case of GISS-E2-R-P1 (Fig. 2l) and INM-CM4 models (Fig. 2v). Therefore, although some biases in CMIP5 AOGCMs do occur for Southern African rainfall, these models do reproduce realistic annual cycles and in general correct austral summer rainfall spatial patterns.

3.2. ENSO variability

Several studies (Federov and Philander, 2001; Wittenberg et al. 2006) suggest that accuracy of the mean state is critical for successful ENSO simulation. To obtain an optimal representation of the full ENSO spatial pattern during austral summer, we decompose the tropical Pacific SST (35°S–35°N/120°E–60°W) into unrotated empirical orthogonal functions (EOFs; Preisendorfer 1988) after linearly detrending the data. Principal components (PC)-based indices of the ENSO mode of variability, which contain less noise, are thus calculated between 1950 and 2005. This procedure allows each model, as well as observation, to exhibit their own ENSO patterns, as opposed to an imposed structure given by an index in specific domain (Saji et al. 2006; Cai et al. 2009; Weller and Cai 2013).

Ability of CMIP5 models to reproduce a correct ENSO pattern is summarized in Figure 3. Figure 3a-b displays the 1st EOF extracted from observation (total fraction of variance about 54.36%) and from the multimodel mean of individual CMIP5 models (total fraction of variance about 41.12%). DJF ENSO SST patterns seem correctly reproduced in CMIP5 models (Fig. 3b). SST anomalies extending along the equator westward from the South American Coast are surrounded by the classic "horseshoe" pattern of opposite sign.

The interannual variance of the ENSO indices in the individual CMIP5 models are similar to observations (Fig. 3c), albeit with a slight underestimations in most CMIP5 models. This agrees with Michael et al. (2013) who showed that interannual time-scales of the observed ENSO variability identified by Rasmussen (1991) are nevertheless well reproduced in CMIP5 models.

CMIP5 models also show good skills in reproducing DJF spatial mean patterns of ENSO (Fig. 1d). The spatial correlation between model outputs and observed rainfall is always higher than 0.6, and can reach more than 0.9 (Fig. 1c). The mean biases are between 0.4 and 0.8°C (Fig. 1d). In most of CMIP5 models, the magnitude (SD) of ENSO patterns is however lower than in observation (Fig. 1d). These biases of ENSO patterns are analyzed more objectively and summarized by looking at the differences between the CMIP5 multimodel mean and observed ENSO components (Fig. 1e). According to numerous studies, ENSO CMIP5 patterns exhibit biases in three areas, and were quite prevalent in the CMIP3 experiment (*e.g.*, AchutaRao and Sperber 2006; Capotondi et al. 2006; Lin 2007). The CMIP5 models however display an encouraging 30% reduction of pervasive cold bias in the western Pacific (Bellenger *al*. 2013). Abnormal westward extension of ENSO patterns is a common and main feature of all CMIP5 models. These differences between GCMs and observation are characterized by overestimations over the western regions (*i.e.*, locations of the observed “horseshoe” anomalies) and underestimation over the eastern regions (Fig. 1e). Such anomalies are much more pronounced in individual models than in the CMIP5 multimodel mean, and exacerbated in CSIRO-Mk3-6-0, GISS-E2-R-P1 and INM-CM4 (not shown). We note that the warm biases in the equatorial Pacific, resulting in the wrong “double ITCZ” (Lin 2007; Ashfaq et al. 2010; Widlansky et al. 2012), are not identified in most CMIP5 models using EOF decompositions, and thus are not observed in the multimodel mean. Underestimation of SST anomalies east of California and Baja peninsula is also identified (Fig. 1e). Such differences are comparatively far less in CNRM-CM5 and MIROC5 (not shown).

As proposed by Rowell (2013), such biases in the simulated ENSO variability can impact the teleconnection with Southern African rainfall in three distinct ways: i) erroneous forcing of the atmosphere overlying the oceanic source of the teleconnection, either due to an incorrect response of surface fluxes or boundary layer processes, ii) an erroneous representation of the atmospheric bridge from the oceanic region to the African region and iii) an erroneous rainfall response over some African regions.

4. Influence of ENSO on summer South African rainfall

Correlation patterns between PC-based ENSO indices and Southern African rainfall from CMIP5 models and observation are performed and displayed in Figures 3 and 4. Note that the statistical significance is computed according to the Student's *t*-test after re-calculating the degrees of freedom with estimated decorrelation scales.

We first compare the correlation patterns from observation and, through the multimodel mean, from CMIP5 models (Fig. 3). As proposed by a number of authors (*e.g.*, Ropelewski and Halpert 1987 1989; Lindesay 1988; Mason and Jury 1997; Kruger 1999; Richard et al. 2000), significant anti-correlation between ENSO and South African rainfall is detected from the observation (Fig. 3a). El Niño events tend to be associated with dry conditions over Southern Africa (Rouault and Richard 2005). In phase summer relationships, which appear significant between 1982 and 2009 (Philippon et al. 2012), are identified over the Western Cape (Fig. 3a). The CMIP5 multimodel mean highlights a good skill in simulating the anti-correlation over the south-eastern regions, but some uncertainties are identified over the north-eastern regions (Fig. 3b). Meanwhile, finer resolutions of CMIP5 models will be required to capture the relationship between ENSO and Western Cape rainfall.

Figure 4 displays the summer-month correlation patterns between ENSO and South African rainfall in the individual CMIP5 models. Statistically, correlation patterns are indistinguishable from random noise in HadGEM2-CC (Fig. 4i) and MRI-CGCM3 (Fig. 4r). Most of the CMIP5 models display a wrong correlation between ENSO and Southern African rainfall over the southwestern and northeastern regions. This is especially the case in ACCESS1-0 (Fig. 4a), CanESM2 (Fig. 4d), CCSM4 (Fig. 4e), FGOALS-g2 (Fig. 4h), IPSL-CM5A-LR and -CM5B-LR (Fig. 4l, n), MRI-ESM1 (Fig. 4s) and all NorESM1 models (Fig. 4t-v).

In summary, CMIP5 biases of South African rainfall seem closely related to differences in simulating ENSO teleconnections. Positive and negative correlation, respectively, between northeastern and southwestern regions could be associated with overestimations and underestimations of northeastern South African and Western Cape rainfall. Better simulations of ENSO-South African rainfall teleconnections are observed where Pacific SST biases are lowest, such as in MIROC5.

5. El Niño anomalies of the austral summer atmospheric circulations

5.1. Near-surface circulation anomalies

Composite maps of anomalies of sea-level pressures (SLPs) during El Niño events are displayed in Figure 6 for NCEP-1 reanalysis and CMIP5 multimodel mean. Higher than normal pressure in tropical and subtropical regions and lower than normal pressure in temperate regions are observed during El Niño using NCEP-1 reanalysis (Fig. 6a). Higher than normal pressure inhibit rainfall and also lead to a change in general circulation of air masses. High pressure anomalies prevent rainfall in general and could reduce the diurnal cycle of rainfall (Rouault et al. 2012). Changes in general circulation modulate precipitation through their impacts on moisture transport (Rouault et al. 2003, Vigaud et al. 2007, 2009), surface convergence (Cook et al. 2000 2001) and by changing the preferred location of rain bearing systems such as cut-off low (Favre et al. 2012) or Tropical Temperate Trough (Hart et al. 2010 2012a, b; Vigaud et al. 2012; Macron et al. 2014). During El Niño years, both intensification and northward shift of the Santa Helena and Indian Ocean subtropical Highs are documented (Cook et al. 2004; Vigaud et al. 2009). Anomalous high pressure is also identified over the north-eastern part of Southern Africa (Fig. 6a), where rains are associated with the southernmost position of the ITCZ.

The CMIP5 multimodel mean highlights a good skill in simulating high pressure anomalies in tropical and subtropical regions and low pressure anomalies in temperate regions (Fig. 6a). Underestimations of low pressure anomalies south-east and south-west of Southern Africa, *i.e.*, from the Santa Helena and Mascarene Highs are revealed. Meanwhile the South Atlantic and continental high pressure anomalies are also underestimated. For instance, changes of Santa Helena High pressure system during El Niño are not simulated in BCC-CSM1.1 (Fig. 7c), CSIRO-MK3-6-0 (Fig. 7g), GISS-E2-R-P1 (Fig. 7k), IPSL-CM5A-LR or -CM5B-LR (Fig. 7l, n) and INM-CM4 (Fig. 7v). This could explain why dry condition over Southern Africa is not correctly reproduced. High pressure anomalies are too strong over the indo-austral ocean in CCSM4 (Fig. 7a), FGOALS-g2 (Fig. 7h), all NorESM1 models (Fig. 7t-u), and CESM1-WACM (Fig. 7w).

5.2. Mid-tropospheric circulation anomalies

El Niño anomalies of geopotential height at 500 hPa (z500) over the southern hemisphere are displayed in Figure 8 using NCEP-1 reanalysis and the CMIP5 multimodel mean. During El Niño years, anomalous high and low pressures are found over the tropical, subtropical regions and low latitude regions using NCEP-1 (Fig. 8a) and seem to mimic the SLP anomalies. Such anomaly indicates an increase of mid-troposphere pressure gradient over a large part of the southern hemisphere, and is associated with an increase of westerly winds in temperate regions brushing of Southern Africa (Fig. 8a). The high pressure anomalies observed near Namibia and southern Angola act to weaken the continental low (Fig. 8a), and potentially prevent rainfall for the same reason mentioned before. In the Austral Ocean region SLP and z500 anomalies (Fig. 6a, 8a) show an equatorward expansion of mid-latitude westerlies and an increased tendency for drier South Atlantic air-mass to be advected over Southern Africa, consistent with earlier conceptual model of Tyson (1986). However, although westerly are found at lower latitude than normal during ENSO, westerly flow veers southwards after reaching the Southwest Africa. This would create lesser convergence with the oncoming easterly flow from the Indian Ocean which is also weakened, both effect reducing continental convergence of moist air and would decrease rainfall.

z500 anomalies from CMIP5 models are very similar to that observed in the near-surface, and thus reveal similar mismatch with NCEP-1 reanalysis (Fig. 6-8). Weaknesses in simulating high pressure anomalies are found over the South Atlantic and the Southern African continent (Fig. 8b). Meanwhile, underestimations of low pressure anomalies of Santa Helena and Mascarene High are identified (Fig. 8b). By looking at El Niño composite anomalies from some selected individual CMIP5 models, this would be due to strong intermodel inconsistencies in reproducing the location of such anomalies. Only CNRM-CM5 and MIROC5 clearly display correct anomalies of Santa Helena and Mascarene Highs (not shown). In other models (not shown), these signals are shifted eastward (e.g. INM-CM4), westward (e.g. ACCESS1-0) or southward (e.g. IPSL-CM5A-MR). ENSO related change in the westerly flow is thus correctly reproduced but with regional biases affecting neighboring regions of Southern Africa. Substantial regional inter-model variability of mid-latitude westerly tracks is therefore expected.

5.3. Large-scale and regional convection anomalies

Tropical and extratropical deep convection is estimated using DJF NCEP-1 Outgoing Longwave Radiation (OLR). Strong negative OLR anomalies (in green) are associated with higher than normal clouds while positive anomalies (in grey) refer to suppressed convection (Fig. 9). Southern African summer rainy season is related to negative OLR anomalies (*i.e.*, increase convection) in Southwest Southern Africa extending over the mid-latitudes (Fig. 9a), and can thus be considered as a precursor of tropical-temperate-troughs (TTTs). Indeed, a significant amount of summer rainfall over Southern Africa is attributed to the occurrence of TTTs (Harrison 1984 1986, Hart 2012a, 2012b), During TTT events, convection over the continent is linked to the transients in the mid-latitudes, resulting in the presence of a convective cloud-band and rain elongated along NW-SE direction (Fig. 9a). These TTTs are related to the establishment of the so-called South-Indian Convergence Zone (SICZ in Figure 9a; Cook, 2000). Meanwhile, summer rainfall in the northern part of austral Africa and Madagascar are associated with the southernmost position of the ITCZ. We have therefore examined whether these two convective patterns could be sensitive to biases of CMIP5 models in simulating the ENSO South African rainfall teleconnection.

Figure 9b displays composite DJF anomalies of OLR values during El Niño years in the NCEP-1 reanalysis. At the southern hemisphere scale, El Niño years are associated with a west-east contrast of suppressed deep-convection over the maritime continent and enhanced convections from the central to eastern Pacific (Fig. 9b). Suppressed deep-convections are also seen over the South Pacific Convergence Zone and the equatoward-shifted ITCZ (Fig.

9b). For Southern Africa, El Niño anomalies are associated with a large band of suppressed convection being surrounded to the east and to the west by enhanced deep-convection both extending in a NW-SE direction (Fig. 9b) suggesting a shift in the SICZ and preferred location of the cloud band. According to Cook (2001), a suppressed convection, probably due to an eastward shift of the SICZ occurs over the northeastern regions of South Africa, Mozambique and South part of Madagascar (Fig. 9b).

Through a CMIP5 multimodel mean, global anomalous convective pattern are correctly identified (Fig. 9c). However, following the SST biases (Figs. 3 and 11), the CMIP5 models shift westward the enhanced deep-convection from the central to the eastern Pacific (Fig. 9c). This appears to have substantial impact over Southern Africa and Southern part of Madagascar in reducing eastward shift of the SICZ (Fig. 9c). Analysis of OLR composites from individual models confirms such global strengths and regional weaknesses of CMIP5 models (Fig. 10). Large-scale anomalous convection patterns are well reproduced over the Pacific Ocean in all CMIP5 models, but with the abnormal westward shift of ENSO patterns. Convection anomalies from Southern Africa and adjacent oceans differ from one model to another. Numerous models show a westward extension of suppressed deep-convection in the ITCZ and Africa, such as ACCESS1-0 (Fig. 10a), BCC-CSM1.1 (Fig. 10c), CanESM2 (Fig. 10d), CCSM4 (Fig. 10e), IPSL-CM5B-LR (Fig. 10n), all NorESM1 models (Fig. 10t-u), INM-CM4 (Fig. 10v), CESM1-WACM (Fig. 10w). Eastward shifts of the SICZ do not occur and deep-convection tends therefore to be favored over the northeastern regions of Southern Africa which explained the wrong correlation with ENSO discussed previously. Other models, such as CNRM-CM5 (Fig. 10f), CSIRO-Mk3-6-0 (Fig. 10g), MIROC5 (Fig. 10o), MPI-ESM-P (Fig. 10p) reproduce correctly and underestimate convective anomalies along the

ITCZ between Africa and the Indian Ocean. In those models, eastward shifts of SICZ are well-simulated, and suppressed deep-convection is identified over Southern Africa.

6. El Niño related SST anomalies

To understand why the ENSO-rainfall teleconnection is not properly represented, we examine the skill of CMIP5 models to reproduce the impact of ENSO on adjacent oceans. In observations, a positive significant correlation between PC-based ENSO indices and Indian Ocean SSTs is identified (Fig. 11a). In other words, the Indian Ocean warms during El Niño and cools during La Nina (Klein et al. 1999). Richard et al. (2000) pointed out that, since 1970, El Niño events embedded in a warmer Indian Ocean SST context are associated with dry conditions over Southern Africa, and hypothesize that El Niño and a warmer Indian Ocean collaborate to create subsidence above Southern Africa. Moreover, an eastward shift of the SICZ is forced by warm anomalies in the tropical south Indian Ocean leading to a weakened subtropical high belt at the longitude of Madagascar and a lesser moisture flux towards Southern Africa coming from south of Madagascar. As illustrated through the CMIP5 multimodel mean, the change in the Indian Ocean that occurs during ENSO is shifted westward compared to the observed SST pattern (Fig. 11). This is clearly identified in all ACCESS models (Fig. 12a-b), BCC-CSM1.1 (Fig. 12c), CCSM4 (Fig. 12e), FGOALS-g2 (Fig. 12h), all NorESM1 models (Fig. 12u-t), INM-CM4 (Fig. 12v), CESM-WACM (Fig. 12w). It could be due to the abnormal westward extensions of ENSO modes in most CMIP5 models (Fig. 11b). Even more important, outside equatorial latitudes, most of the CMIP5 models highlight weaker correlations over the Indian Ocean than in observation (Fig. 11b, 12). The warming of Indian Ocean during El Niño event would be much less important in CMIP5 models than in observation. This could explain why eastward shifts of the SICZ are less important in CMIP5 models and why high pressure anomalies are not reproduced by the models. Thus, regarding the Indian SST-ENSO correlation patterns, better matches with observations are identified in CNRM-CM5 (Fig. 12f), MIROC5 (Fig. 12o), all MPI-ESM models (Fig. 12p-q).

7. Discussion and Conclusion

This study has provided an overview of the capability of CMIP5 coupled models to represent the impact of ENSO on Southern African summer rainfall. Such teleconnections are influenced by biases in the spatiotemporal variability of ENSO and by an erroneous rainfall response over Southern Africa to ENSO. The CMIP5 experiments show a realistic seasonal rainfall cycle. Interannual variability of rainfall is almost always underestimated while total DJF rainfall is overestimated. Numerous weaknesses in simulating ENSO spatiotemporal variability are still present in most CMIP5 models and do not differ much from CMIP3 experiments (*e.g.,* AchutaRao and Sperber 2006; Capotondi et al. 2006; Lin 2007; Bellenger et al. 2013). Especially, westward extensions of ENSO modes of variability are likely to disrupt the atmospheric bridge from the Indo-Pacific region to the South African region.

As calculated by three metrics in Figure 13, better skill in simulating El Niño dry anomalies throughout South Africa is performed in CNRM-CM5, MPI-ESM-P and, looking through the spatial correlation, in MIROC5. Meanwhile, CMIP5 models with lowest skills, such as CanESM2, IPSL-CM5A-LR and INM-CM4, show anomalous wet conditions northeastern part of Southern Africa. This is due to CMIP5 model shortcomings in simulating ENSO-like anomalies of SLP, deep-convection and SST between the Atlantic and Indian oceans, and more particularly their spatial patterns (Figure 13). From the near-surface to the mid-troposphere, the best CMIP5 models, *i.e.*, CNRM-CM5, HadGEM2-ES and all MPI models, reproduce the shift and change in high pressure affecting the latitudinal location of the mid-latitude westerly tracks over the South Atlantic and South Indian Oceans. The mean relative bias, which is highlighted from models showing standardized biases close to zero in Figure 13, affect the shift in pressure over the tropical and subtropical South Atlantic (including the continent) and, thus, could affect the eastward ridging of the Santa-Helena High. Meanwhile, CSIRO-Mk3-6-0, HadGEM2-CC, and CESM1-WACM, which present very odd rainfall patterns, show lowest skills in simulating El Niño SLP anomalies (Fig. 13). In modelling high-pressure over the continent, such odd SLP anomalies can however lead to a false-good reproduction of the ENSO-South African rainfall correlation, for instance in HadGEM2-CC (Fig. 13). Large-scale tropical anomalies of deep-convection over the maritime continent and enhanced convection from the central to eastern Pacific are simulated in CMIP5 models and closely follow the SST biases. Meanwhile, large differences between models occur above Africa and the adjacent oceans due to difficulties in simulating a warm Indian Ocean during El Niño events. Indeed, better skills of CMIP5 models, as seen from CNRM-CM5, all MPI models and MIROC5, occur when eastward shifts of the SICZ and warm Indian SSTs are identified (Fig. 13). The CMIP5 biases therefore affect the longitudinal location of the SICZ, and probably also the position of TTT development. Note however that, although GISS-E2-R-P1 is able to reproduce the warmer Indian SST and the eastward shift of the SICZ, weaknesses in simulating South Atlantic and continental SLP anomalies lead to poor ENSO-rainfall correlation patterns (Fig. 13). This pattern is therefore associated to underestimations of Southern African rainfall in the northernmost regions. The CMIP5 biases in simulating El Niño SLP and z500 anomalies over the South Atlantic might not be linked to anomalies over the Indian Ocean.

Acknowledgments

MR wants to thanks ACCESS, NRF, WRC and the Nansen Tutu for Marine Environmental Research for funding. BD wants to thanks UCT for his URC research fellowship.

References

AchutaRao K, Sperber KR (2006) ENSO simulation in coupled ocean-atmosphere models: are the current models better? Clim Dyn 27:1–15.

Ashfaq M, Skinner CB, Diffenbaugh NS (2010) Influence of SST biases on future climate change projections. Clim Dyn 36:1303–1319.

Bellenger H, Guilyardi E, Leloup J, Lengaigne M, Vialard J (2013) ENSO representation in climate models: from CMIP3 to CMIP5. Clim Dyn 42:1999–2018.

Camberlin P, Janicot S, Poccard I (2001) Seasonnality and atmospheric dynamics of the teleconnection between African rainfall and tropical sea surface temperature Atlantic vs. ENSO. Int J Clim 21:973–1005.

Capotondi A, Wittenberg A, Masina S (2006) Spatial and temporal structure of tropical pacific Interannual variability in 20th century coupled simulations. Ocean Model 15:274–298.

Cai W, Sullivan A, Cowan T (2009) Rainfall teleconnections with Indo-Pacific variability in the WCRP CMIP3 models. J Clim 22:5046–5071.

Cook KH (2000) The South Indian convergence zone and inteannual rainfall variability over Southern Africa. J Clim 13:3789–3804.

Cook KH (2001) A Southern Hemisphere wave response to ENSO with implications for southern Africa precipitation. J Atmos Sci 15:2146–2162.

Cook KH (2004) Wet and dry spells within particularly wet and dry summers in the South African summer rainfall region. Clim Res 26:17–31.

Fauchereau N, Pohl B, Reason CJC, Rouault M, Richard Y (2009) Recurrent daily OLR patterns in the Southern Africa/Southwest Indian Ocean region, implications for South African rainfall and teleconnections. Clim Dyn 32:575–591.

Favre A, Hewitson B, Tadross M, Lennard C, Cerezo-Mota R (2012) Relationships between cut-off lows and the semiannual and southern oscillations. Clim Dyn 38:1473–1487.

Federov AV, Philander SG (2001) A stability analysis of the tropical ocean-atmosphere interactions: bridging measurements of, and theory for El Niño. J Clim 14:3086–3101.

Harris I, Jones PD, Osborn TJ, Lister DH (2014) Updated high-resolution grids of monthly climatic observations - the CRU TS3.10 Dataset. Int J Clim 34:623–642.

Harrison MSJ (1984) A generalised classification of South African summer rain bearing synoptic systems. J Climatol 4:547–560.

Harrison MSJ (1986) A synoptic climatology of South African rainfall variations. PhD thesis. University of Witwatersrand, Johannesburg, 341p.

Hart NCG, Reason CJC, Fauchereau N (2010) Tropical-extratropical interactions over southern Africa: three cases of heavy summer season rainfall. Mon Wea Rev 138:2608–2623.

Hart NCG, Reason CJC, Fauchereau N (2012a) Cloud bands over southern Africa: seasonality, contribution to rainfall variability and modulation by the MJO.

Hart NCG, Reason CJC, Fauchereau N (2012b) Building a tropical extratropical cloud band metbot. Mon Wea Rev 140:4005–4016.

Joly M, Voldoire A, Douville H, Terray P, Royer J-F (2007) African monsoon teleconnections with tropical SSTs : validation and evolution in a set of IPCC4 simulations. Clim Dyn 29:1–20.

Kalnay E, Kanamistsu M, Kistler R, Collins W, Deaven D, Gandin L, Iredell M, Saha S, White G, Woolen J, Zhu Y, Chelliah M, Ebisuzaki W, Higgins W, Janowiak J, Mo KC

Ropelewski C, Wang J, Leetma R, Reynolds R, Jenne R, Joseph D (1996) The NCEP/NCAR 40-year reanalysis project. Bull Amer Met Soc 77:437–471.

Klein SA, Soden BJ, Lau NC (1999) Remote sea surface variations during ENSO: evidence for a tropical atmospheric bridge. J Clim 12:917–932.

Kruger, A.C. (1999). The influence of the decadal-scale variability of summer rainfall on the impact of El-Niño and La Niña events in South Africa. Int J Clim 19:59–68.

Langenbrunner B, Neelin DJ (2013) Analyzing ENSO teleconnections in CMIP models as a measure of model fidelity in simulating precipitation. J Clim 26:4431–4446.

Lin J-L (2007) The double-ITCZ problem in IPCC AR4 coupled GCMs: Ocean-atmosphere feedback analysis. J Clim 20:4497–4525.

Lindesay JA (1988) South African rainfall, the souther oscillation and a souther hemisphere semi-annual cycle. J Climatol 8:17–30.

Macron C, Pohl B, Richard Y (2014) How do Tropical Temperate Troughs Form and Develop over Southern Africa? J Clim 27:1633–1647.

Mason SJ, Jury M (1997) Climatic variability and change over the Southern Africa: a reflection on underlying processes. Prog Phys Geo 21:23–50.

Michael J-P, Misra V, Chassignet EP (2013) The El Niño and Southern Oscillation in the historical centennial integrations of the new generation of climate models. Reg Environ Change 13:121–130.

Mulenga HM, Rouault M, Reason CJC (2003) Dry summers over north-eastern South Africa and associated circulation anomalies. Clim Res 25:29-41.

Nicholson SE (1997) An analysis of the ENSO signal in the tropical Atlantic and western Indian oceans. Int J Clim 17:345–375.

Nicholson SE, Kim J (1997) The relationship of the El Niño-Southern Oscillation to African rainfall. Int J Clim 17:117–135.

Pohl B, Fauchereau N, Richard Y, Rouault M, Reason CJC (2009) Interactions between synoptic, intraseasonal and Interannual convective variability over Southern Africa. Clim Dyn 33:1033–1050.

Phillipon N, Rouault M, Richard Y, Favre A (2012) The influence of ENSO on winter rainfall in South Africa. Int J Clim 32:2333–2347.

Preisendorfer RW (1988) Principal Component Analysis in Meteorology and Oceanography. Elsevier, Amsterdam.

Rasmussen EM (1991) Observational aspects of ENSO cycle teleconnections. In: Teleconnection Lonking Worldwide Climate anomalies: Scientific Basis and Societal Impact [Glantz et al. (eds.)]. Cambridge University Press, United Kingdom and New York, 309–343.

Richard Y, Trzaska S, Roucou P, Rouault M (2000) Modification of the Southern African rainfall variability/El Niño southern oscillation relationship. Clim Dyn 16:883–895.

Richard Y, Fauchereau N, Poccard I, Rouault M, Trzaska S (2001) XXth century droughts in Southern Africa: spatial and temporal variability, teleconnections with oceanic and atmospheric conditions. Int J Clim 21:873–885.

Ropelewski CF, Halpert MS (1987) Global and regional scale precipitation patterns associated with the El Niño/Southern Oscillation. Mon Wea Rev 115:1606–1626.

Ropelewski CF, Halpert MS (1989) Precipitation patterns associated with the high indices phase of the southern oscillation. J Clim 2:268–284.

Rouault M, Florenchie P, Fauchereau N, Reason CJC (2003) South East tropical Atlantic warm events and southern African rainfall. Geophys Res Lett 30:8009. Doi:10.1029/2002GL014840.

Rouault M, Richard Y (2005) Intensity and spatial extent of droughts in Southern Africa. Geophys Res Lett 32:L15702. Doi:10.1029/2005GL022436.

Rouault M, B. Pohl, Penven P (2010) Coastal Oceanic climate change and variability from 1982 to 2009 around South Africa. S Afr J Mar Sci 32(2): 237–246.

Rouault M, Sen Roy S, Balling JRC (2013) The diurnal cycle of rainfall in South Africa in the austral summer. Int J Clim 33:770–777.

Rowell DP (2013) Simulating SST Teleconnections to Africa: What is the state of the Art? J Clim 26:5397–5418.

Saji N, Xie S-P, Yamagata T (2006) Tropical Indian Ocean variability in the IPCC twentieth-century climate simulations. Journal of Climate 19:4397–4417.

Smith T, Reynolds R, Peterson TC, Lawrimore J (2008) Improvements to NOAA's historical merged land-ocean surface temperature analysis (1880-2006). J Clim 21:2283–2296.

Tatebe H, Ishii M, Mochizuki T, Chikamoto Y, Sakamoto T, Komuro Y, Mori M, Yasunaka, S, Watanabe M, Ogochi K, Suzuk, T, Nishimura T, Kimoto M (2012) Initialization of the climate model MIROC for decadal prediction with hydrographic data assimilation. J Meteorol Soc Jpn, 90A:275–294.

Taylor KE (2001) Summarizing multiple aspects of model performance in a single diagram. J Geophys Res-Atmos 106:7183–7192.

Taylor KE, Stouffer RJ, Meehl GA (2012) An Overview of CMIP5 and the experiment design. Bull Amer Meteor Soc 93:485–498.

Todd MC, Washington R (1999) Circulation anomalies associated with tropical-temperate troughts in southern Africa and the southwest Indian Ocean. Clim Dyn 15:937–951.

Todd MC, Washington R, Palmer PI (2004) Water vapour transport associated with tropical-temperate trough systems over Southern Africa and the southwest Indian Ocean. Int J Clim 24:555–568.

Tyson PD (1986) Climatic change and variability in Southern Africa. Oxford University Press, Cape Town.

Vigaud N, Richard Y, Rouault M, Fauchereau N (2007) Water vapour transport from the tropical Atlantic and summer rainfall in tropical southern Africa. Clim Dyn 28 (2-3): 113–123.

Vigaud N, Richard Y, Rouault M, Fauchereau N (2009) Moisture transport between the South Atlantic Ocean and southern Africa: relationships with summer rainfall and associated dynamics. Clim Dyn 32:113–123.

Vigaud N, Pohl B, Crétat J (2012) Tropical-temperate interactions over Southern Africa simulated by a regional climate model. Clim Dyn 39:2895-2916.

Ward (1992) Provisionnaly correctly surface wind data, worldwide ocean-atmosphere surface fields and Sahelian rainfall variability. J Clim 5:454–475.

Weller E, Cai W (2013) Asymmetry in IOD and ENSO Teleconnection in a CMIP5 Model Ensemble and Its Relevance to Regional Rainfall. J Clim 26:5139–5149.

Widlansky MJ, Timmermann A, Stein K, McGregor S, Schneider N, England MH, Lengaigne M, Cai W (2012) Changes in South Pacific rainfall bands in a warming climate. Nature climate change 3:417–423.

Wittenberg AT, Rosati A, Lau N-C, Ploshay JJ (2006) GFDL's CM2 global coupled climate models. Part III: tropical Pacific climate and ENSO. Journal of Climate 19:698–722.

Yang X, DelSole T (2012) Systematic comparison of ENSO teleconnection patterns between models and observations. J Clim 25:425–446.

Yeager S, Karspeck A, Danabasoglu G, Tribbia J, Teng H (2012) A decadal prediction case study: Late twentieth-century North Altantic Ocean heat content. J Clim 25:5173-5189.

Zhang GJ, Wang H (2006) Toward mitigating the double ITCZ problem in NCAR CCSM3. Geophys Res Lett 33:L06709. doi:10.1029/2005GL025229.

Figure and Captions

Table 1. Summarized information on observation data and CMIP5 models used in the study.

Fig 1. Evaluation of model performances. **a** Annual cycle of Southern African rainfall (36°–20°S, 10°–36°E) from CRU TS 3.21 observations (blue), CMIP5 models (grey) and multimodel mean (MMM; red). **b** Coefficient of variation of DJF rainfall time-series from CMIP5 models (grey), the multimodel mean (MMM, red) and observation (blue) over South African region. **c** Taylor diagram of the DJF rainfall spatial patterns from the CMIP5-MMM (red), 24 individual models (grey) and from observations (blue square) over the tropical Pacific. The diagram is a function of the root mean square (RMS, green dashed circles – x-axis), the correlation coefficient (black dashed lines – y-axis) and the standard deviation (blue dashed compared to solid circles – x-axis). Since the values are normalized the reference (observation values) has a standard deviation of 1.

Fig. 2 Summer (DJF) differences between simulated and observed rainfall fields (mm/day) between 1950 and 2005. **a** the CMIP5 multimodel mean (MMM) minus the CRU TS 3.21 observations. **b** Idem for the 24 individual models from CMIP5 experiments. The statistical significance of differences (red dashed contours) has been estimated using a Student *t*-test at $p=0.05$.

Fig. 3 Summer (DJF) ENSO SST mode of variability between 1950 and 2005: CMIP5-MMM vs observations. Empirical Orthogonal Functions (EOFs) of DJF Pacific SSTs using **a** CMIP5 multimodel mean (MMM), **b** ERSST.v3b observation and **e** the difference between the two. **c** Standard deviation of DJF-ENSO principal components (PCs) extracted by EOFs from the CMIP5-MMM (red), 24 individual models (grey) and from observations (blue) over the tropical Pacific, **d** Taylor diagram of the ENSO patterns from the CMIP5-MMM (red), 24 individual models (grey) and from observations (blue square) over the tropical Pacific. The diagram is a function of the root mean square (RMS, green dashed circles – x-axis), the correlation coefficient (black dashed lines – y-axis) and the standard deviation (blue dashed circles compared to solid circle – x-axis). Since the values are normalized the reference (observation values) has a standard deviation of 1.

Fig. 4 Observed and simulated DJF correlations between ENSO and South African rainfall. **a** pointwise correlation between the ENSO component extracted by EOF and South African rainfall in observation and **b** the CMIP5 multimodel mean (MMM). Red dashed contours indicate the 90% confidence level of Pearson's product moment correlation coefficient assuming independent normal distributions.

Fig. 5 a-x Simulated DJF pointwise correlation between the ENSO component extracted by EOF and South African rainfall in the individual models from CMIP5 experiments. Red dashed contours indicate the 90% confidence level of Pearson's product moment correlation coefficient assuming independent normal distributions.

Fig. 6 Observed and simulated El Niño summer anomalies of the surface atmospheric circulation near South Africa. El Niño composite anomalies (*i.e.*, ENSO-PC>0.01) of Sea Level Pressures (in mb) **a** NCEP-1 reanalysis and **b** CMIP5 multimodel mean (MMM). The statistical significance (red dashed contours) has been estimated using a *t*-test at *p*=0.05. This test is applied on zonal and meridional winds for the NCEP-1 composite map.

Fig. 7 SLP summer anomalies near South Africa during El Niño years in the individual CMIP5 models between 1950 and 2005. **a-x** Niño composite anomalies (*i.e.*, ENSO-PC>0.01) of SLPs (in mb) in the individual models from historical runs of CMIP5 models. The statistical significance (red dashed contours) has been estimated using a *t*-test at *p*=0.05.

Fig. 8 Observed and simulated El Niño summer anomalies of mid-tropospheric atmospheric circulation over the southern hemisphere. El Niño composite anomalies (*i.e.*, ENSO-PC>0.01 of z500 (in m) **a** NCEP-1 reanalysis, **b** CMIP5 multimodel mean (MMM) and **c-f** some selected individual models. Wind anomalies (vectors, m.s^{-1}) are only displayed for NCEP-1. The statistical significance (red dashed contours) has been estimated using a *t*-test at *p*=0.05. This test is applied on zonal and meridional winds for the NCEP-1 composite maps.

Fig. 9 Outgoing longwave radiations (OLR) anomalies during austral summer to OLR anomalies during El Niño events. **a** Composite anomalies of OLR (in W.m^{-2}) during austral summer rainfall in South Africa (*i.e.*, DJF rainfall > 1.75mm/month). **b** El Niño composite anomalies (*i.e.*, ENSO-PC>0.01) of OLR **b** in the NCEP-1 reanalysis and **c** in the CMIP5 multimodel mean (MMM). The statistical significance (red dashed contours) has been estimated using a *t*-test at *p*=0.05.

Fig. 10 El Niño summer anomalies of OLR over the southern hemisphere in the individual CMIP5 models. **a-x** El Niño composite anomalies (*i.e.*, ENSO-PC>0.01) of OLR (in W.m^{-2}) in the individual CMIP5 models. The statistical significance (red dashed contour lines) has been estimated using a *t*-test at *p*=0.05.

Fig. 11 Observed and simulated DJF correlations between ENSO components and worldwide SSTs. **a** pointwise correlation between the ENSO components extracted by EOF and SSTs in observation and **b** CMIP5 multimodel mean (MMM). Grey contours indicate the 90% confidence level of Pearson's product moment correlation coefficient assuming independent normal distributions.

Fig. 12 DJF correlations between ENSO components and worldwide SSTs hemisphere in the individual CMIP5 models. **a-x** Pointwise correlation between the ENSO component extracted by EOF and SSTs in the individual CMIP5 models. Grey contours indicate the 90% confidence level of Pearson's product moment correlation coefficient assuming independent normal distributions.

Fig. 13. Ranking of CMIP5 models based on the performances in simulating the different aspects of ocean-atmospheric dynamics related to El Niño-Southern African rainfall teleconnections, and also rainfall over Southern Africa itself. Three metrics quantifying the biases from observations are applied to ENSO-rainfall correlation patterns (36–20°S; 10–38°E), SLP anomalies (0–55°S; 20°W–80°E), OLR anomalies (0–55°S; 20°W–80°E) and ENSO-Indian SST correlation patterns (35°S–30°N; 30°120°E). CMIP5 biases are assessed through the deviations from perfect scores: i) one minus the spatial correlation coefficients between observed and simulated patterns (1-R); ii) since the observed values are normalized (SD=1), the absolute values of one minus the standard deviations of CMIP5; and iii) the root mean square error (RMSE). Each row in the table is then individually standardized to compare the CMIP5 models. Blue (red) squares indicate models showing lower (higher) bias than the multimodel mean. Rank of each model also is displayed for each measurement in the bottom left corner, while all the models are displayed from their general ranking from the left to the right.

Figure 1
Click here to download high resolution image

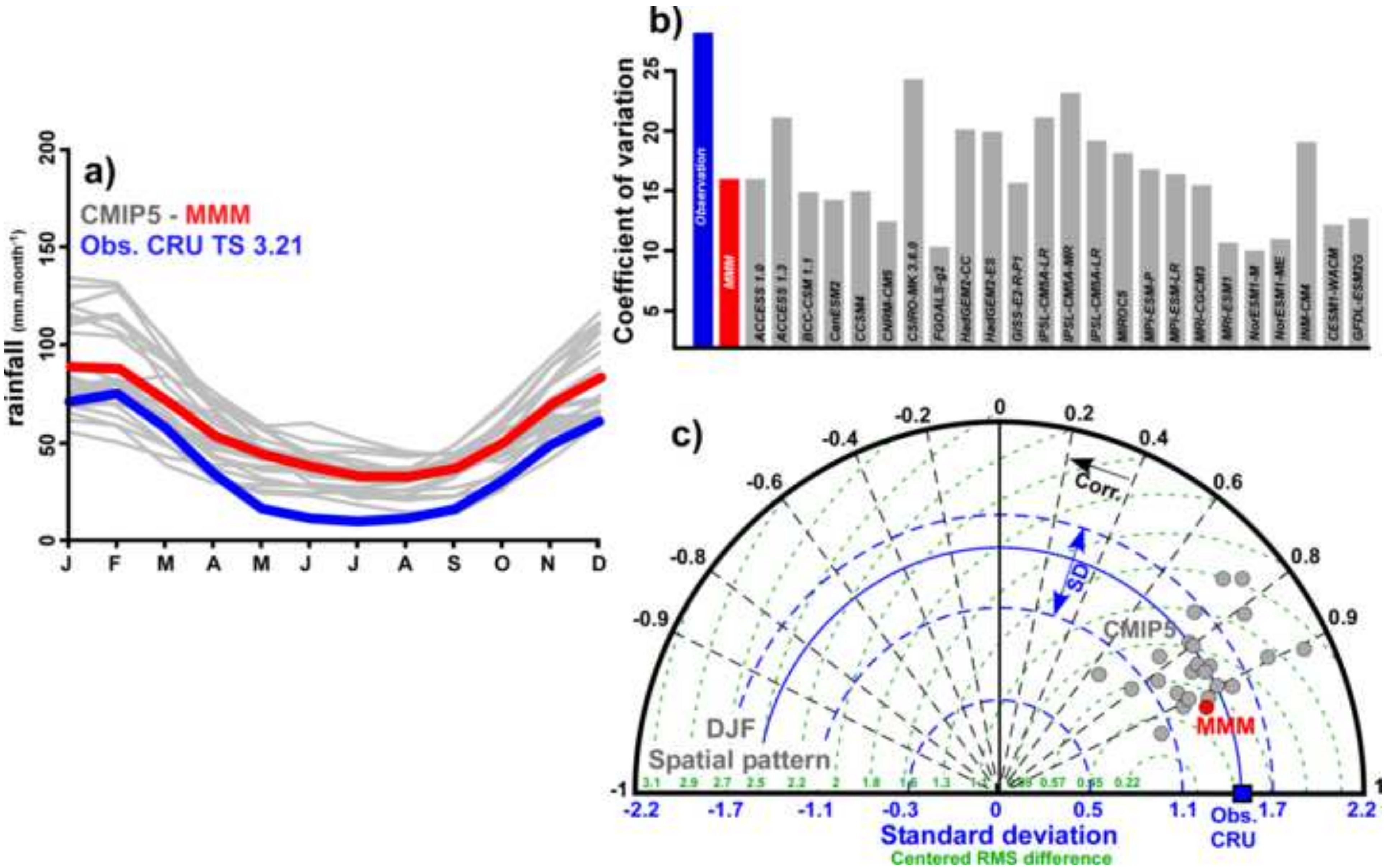

Figure 2

Click here to download high resolution image

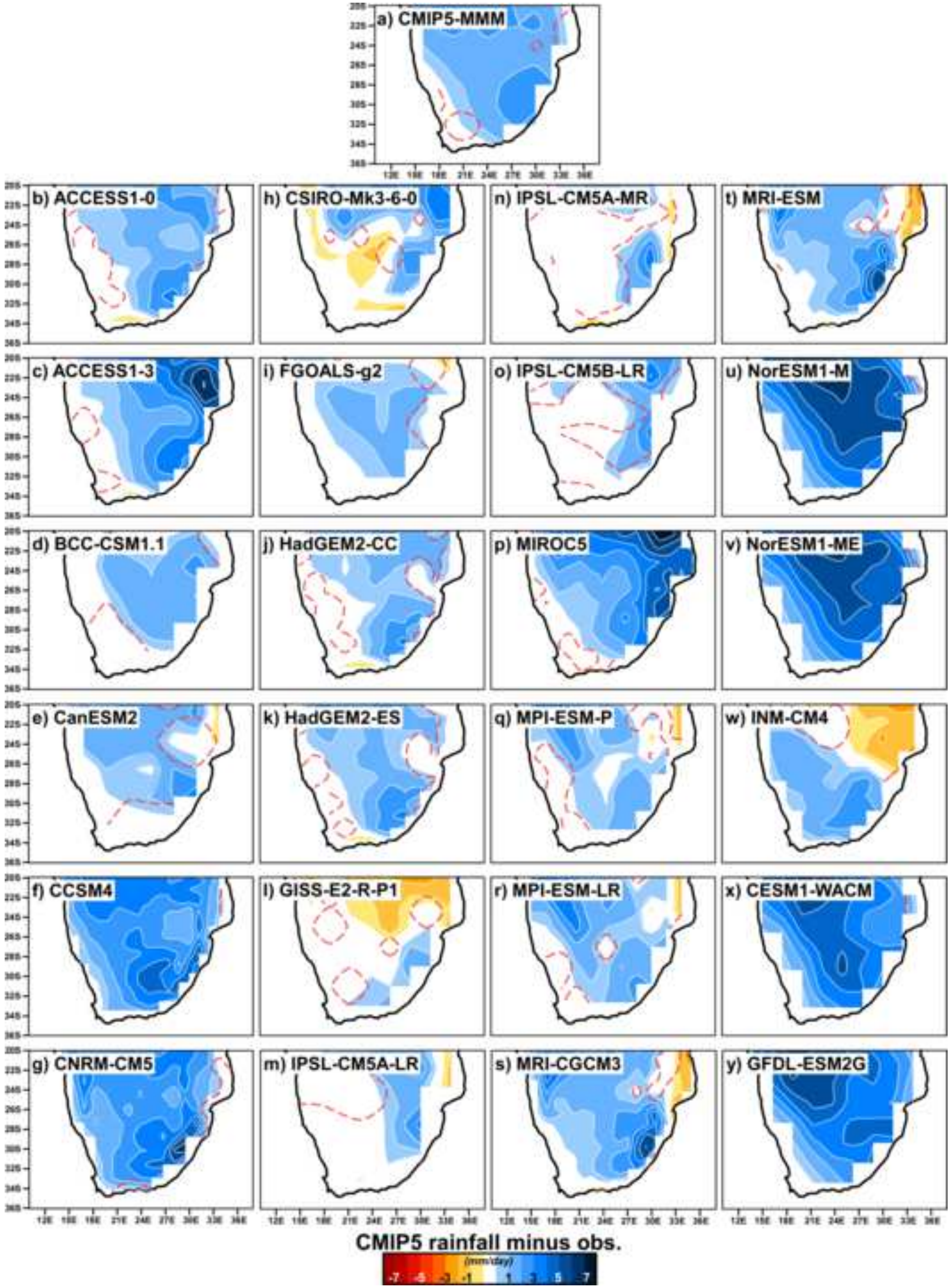

Figure 3

Click here to download high resolution image

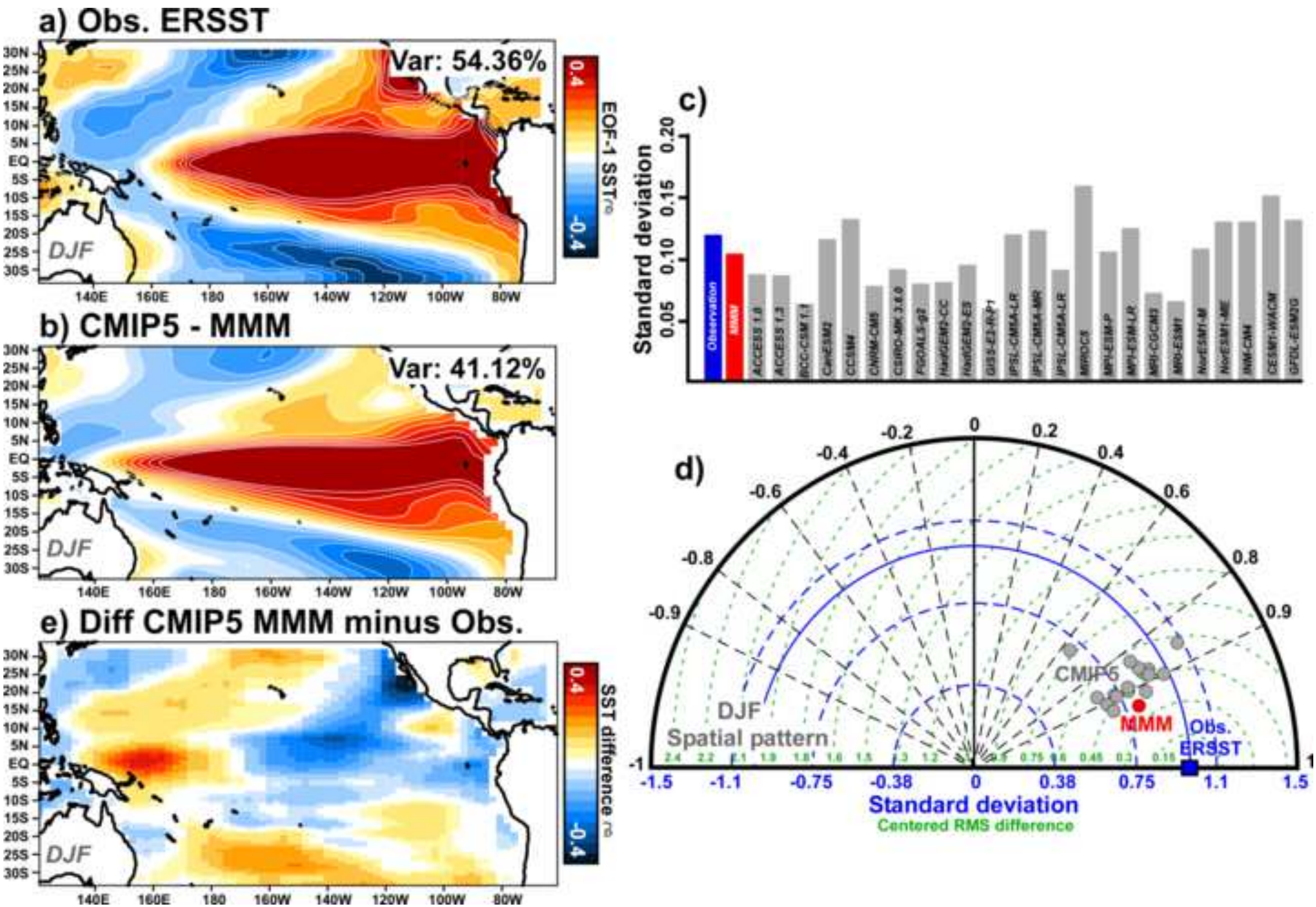

Figure 4
Click here to download high resolution image

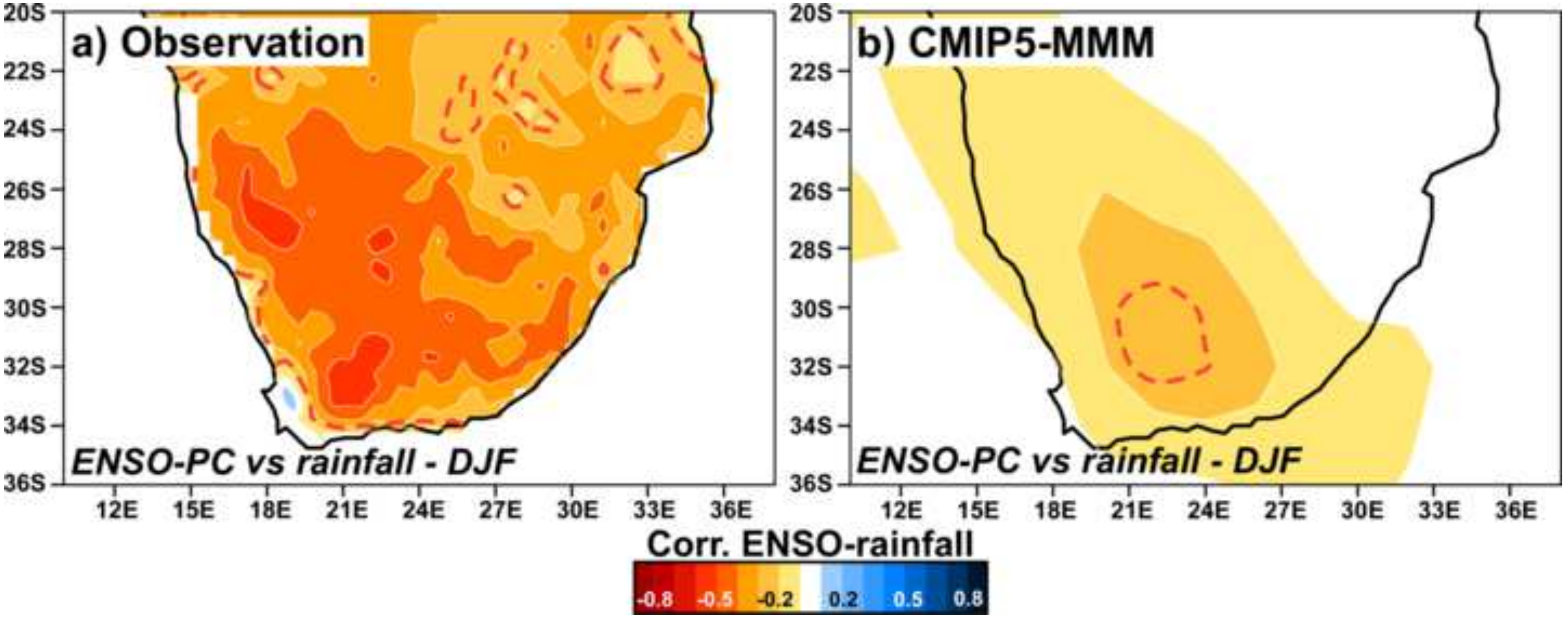

Figure 5
Click here to download high resolution image

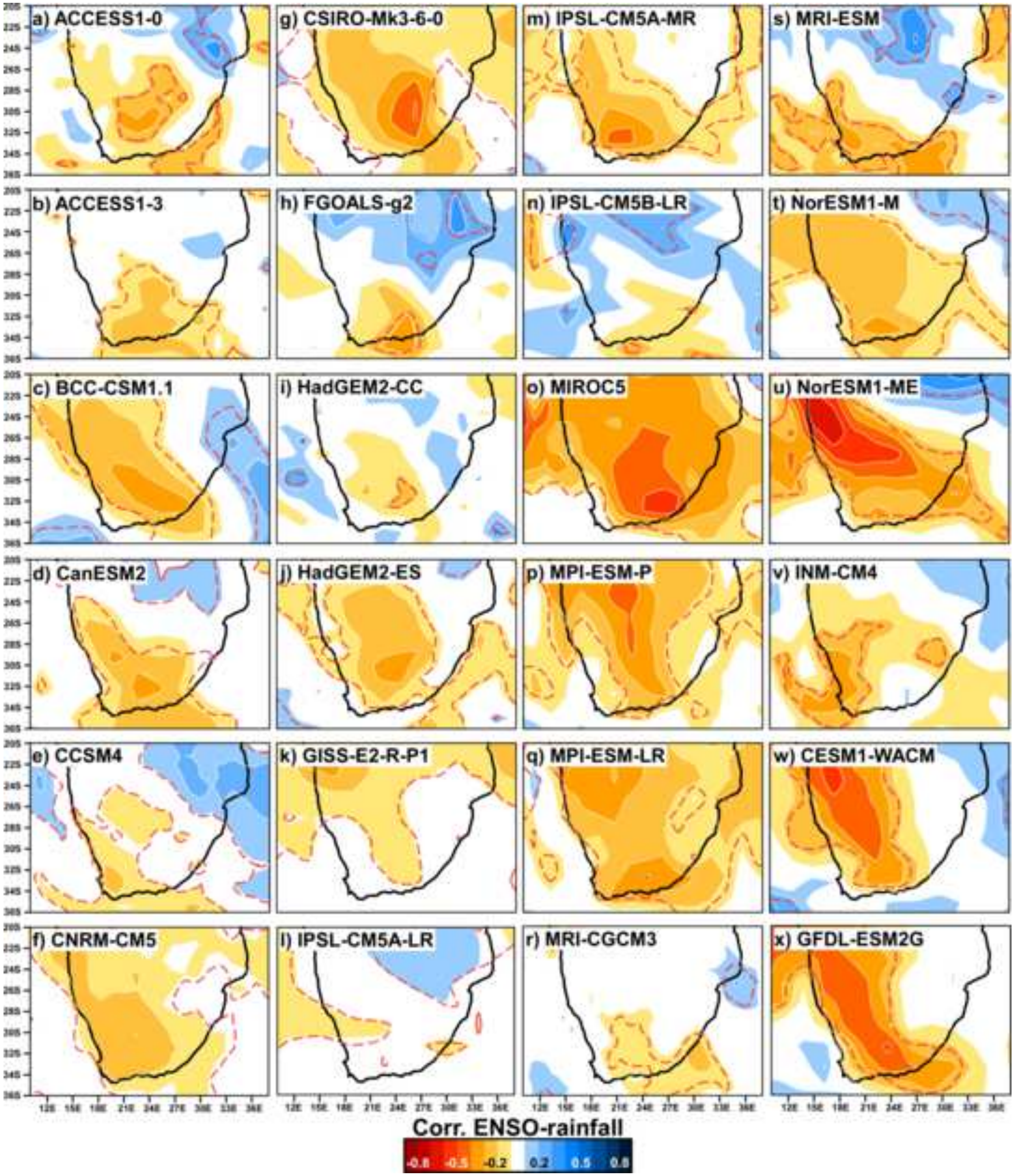

Figure 6
Click here to download high resolution image

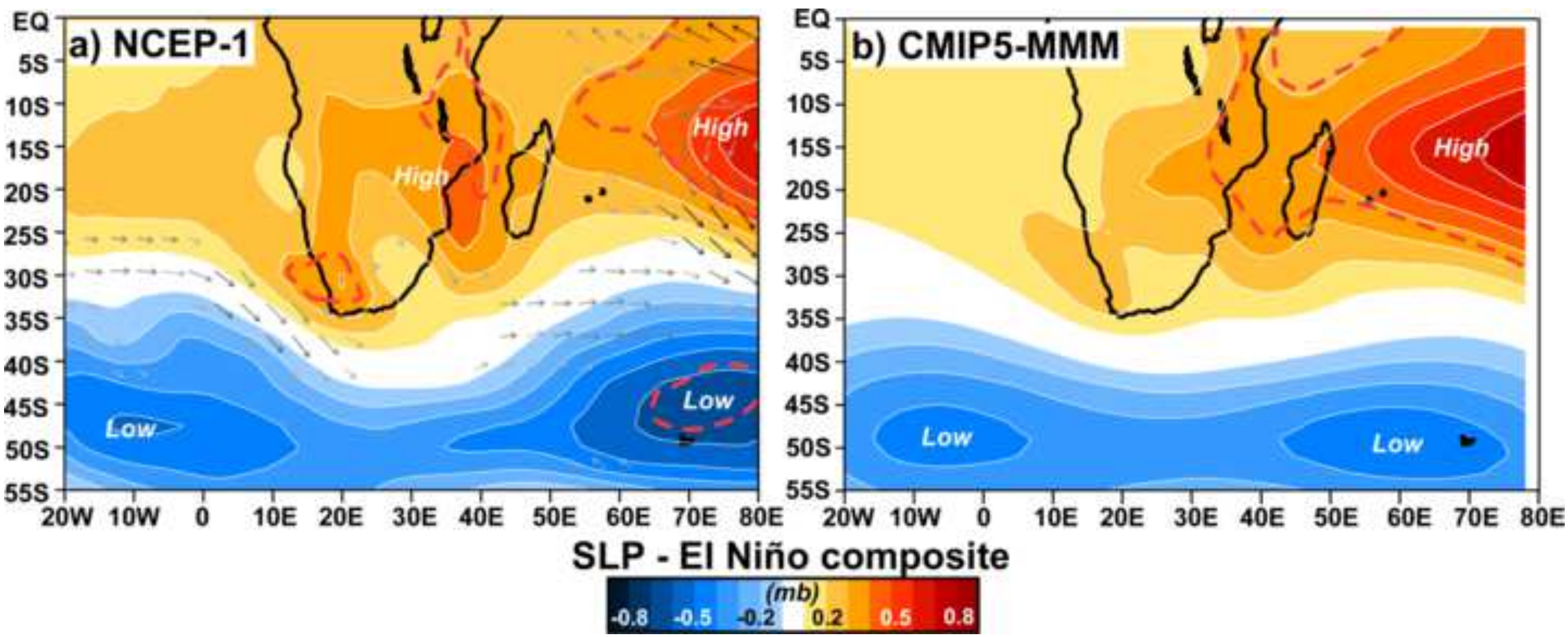

Figure 7
Click here to download high resolution image

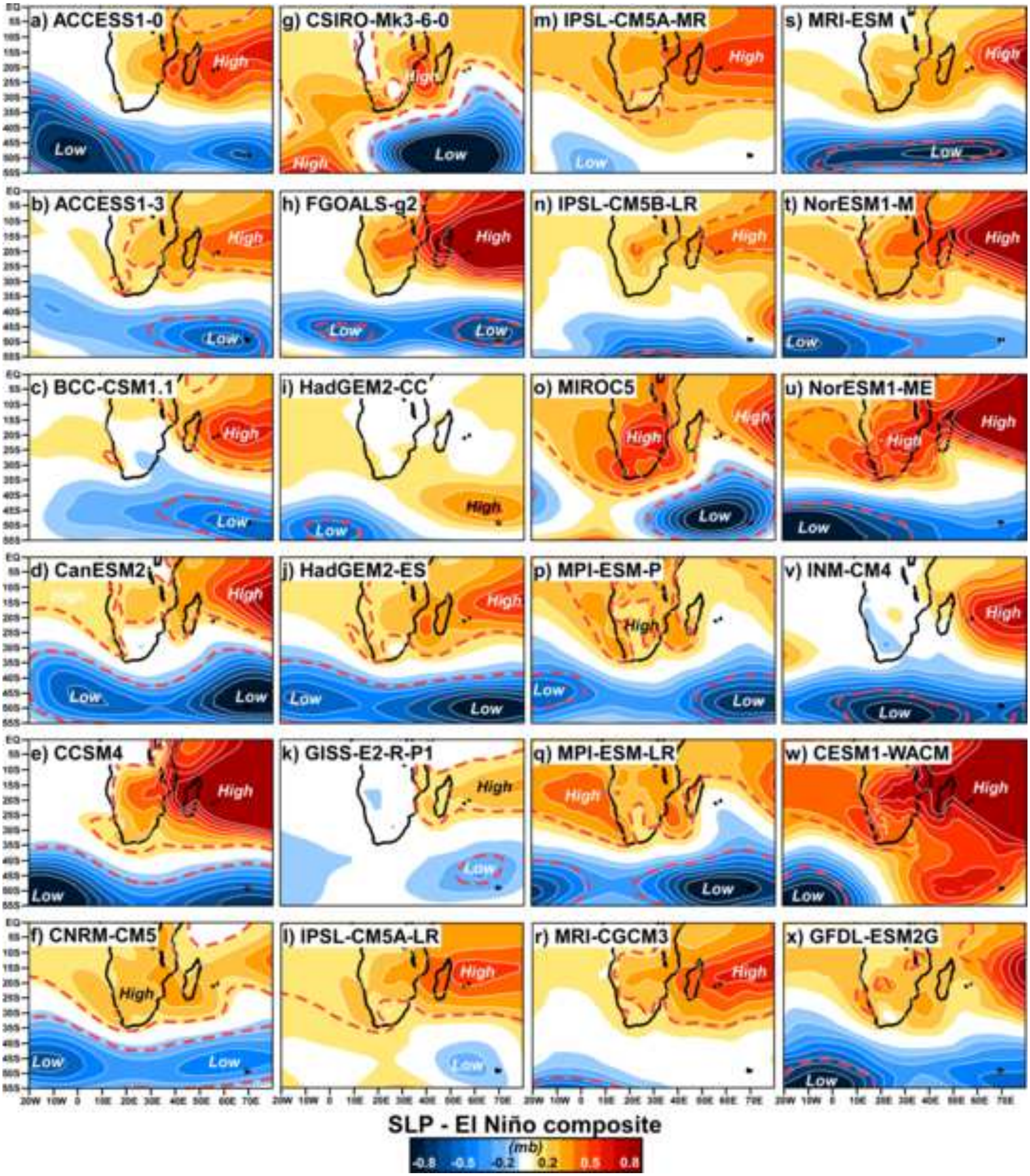

Figure 8
Click here to download high resolution image

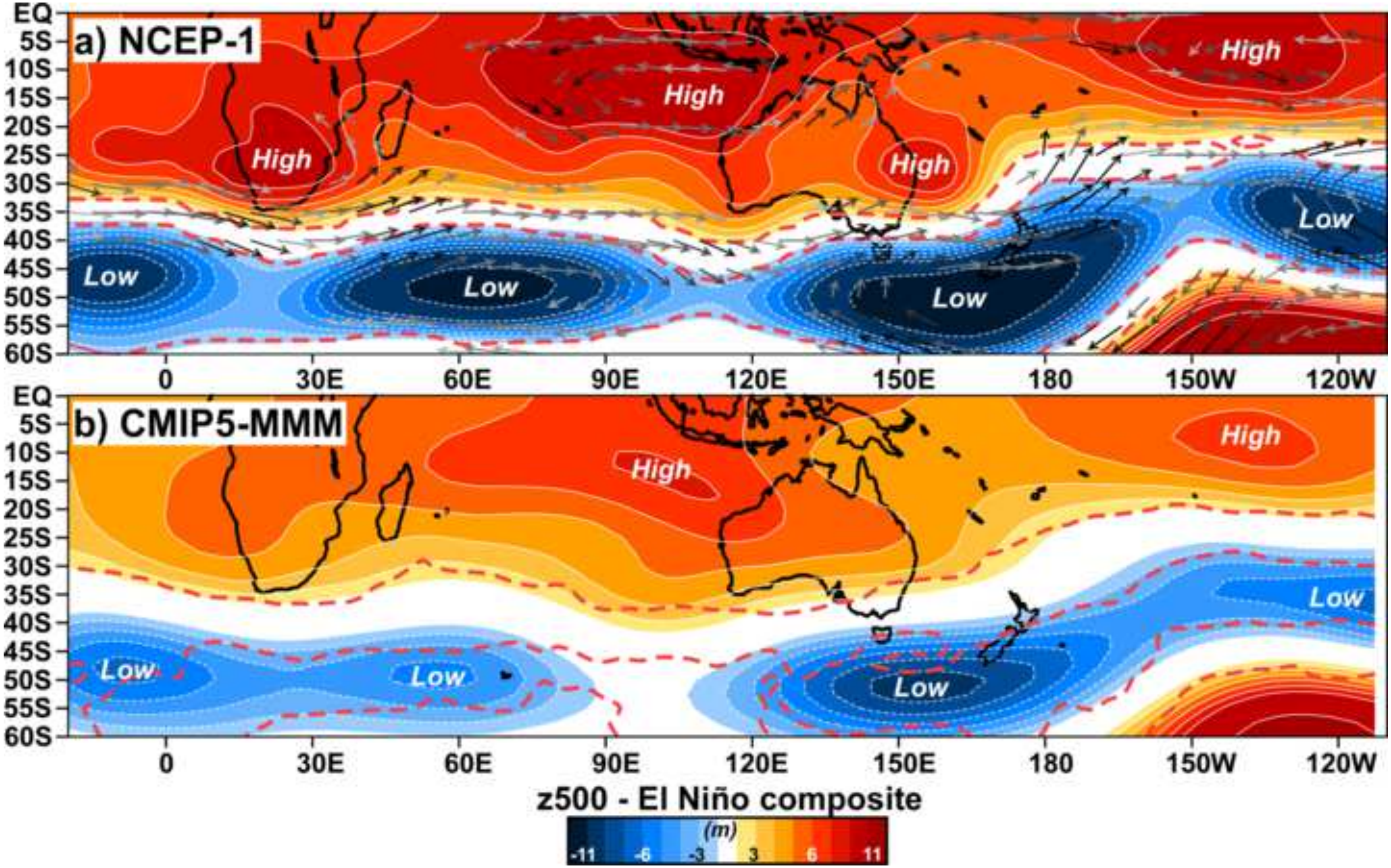

Figure 9
Click here to download high resolution image

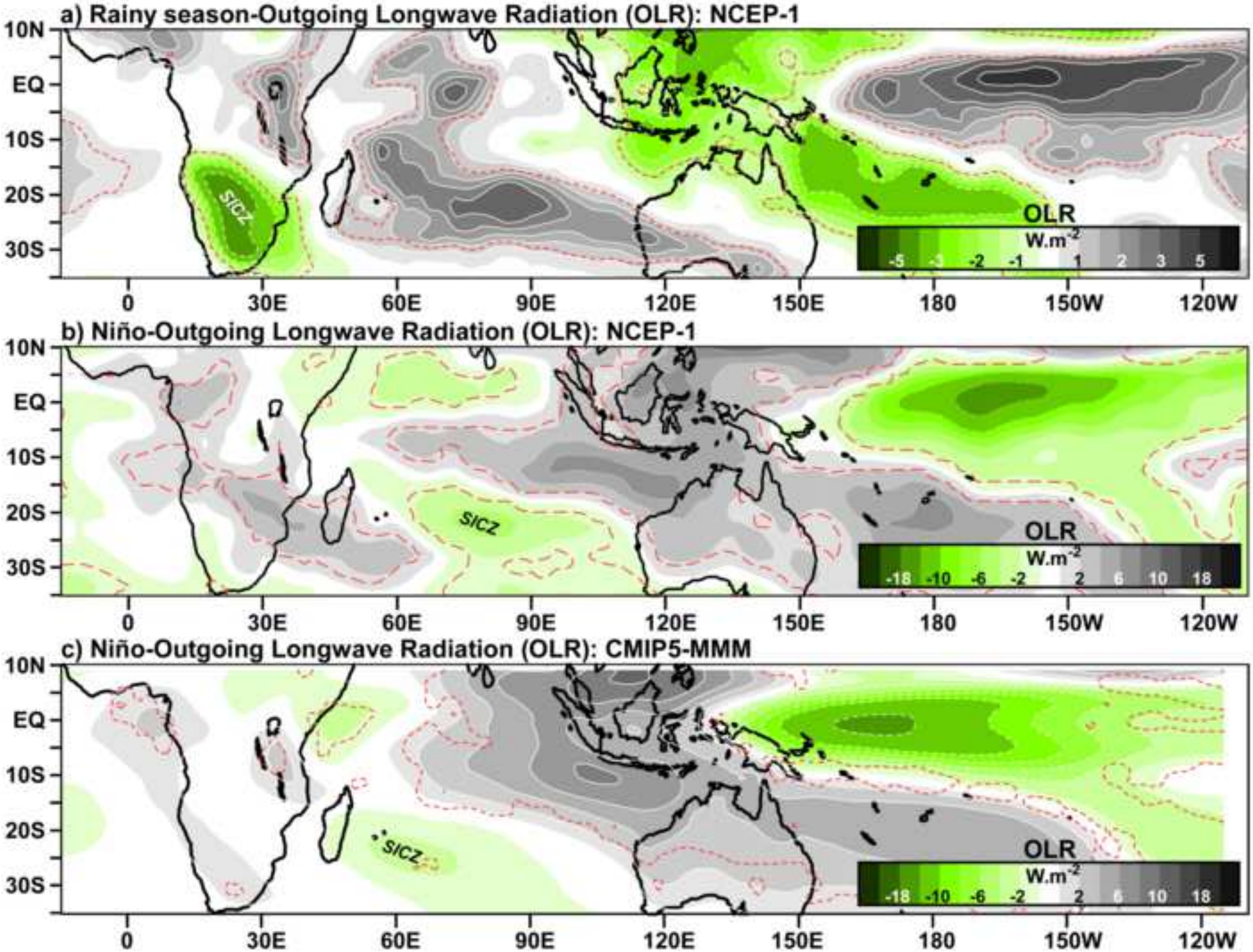

Figure 10

Click here to download high resolution image

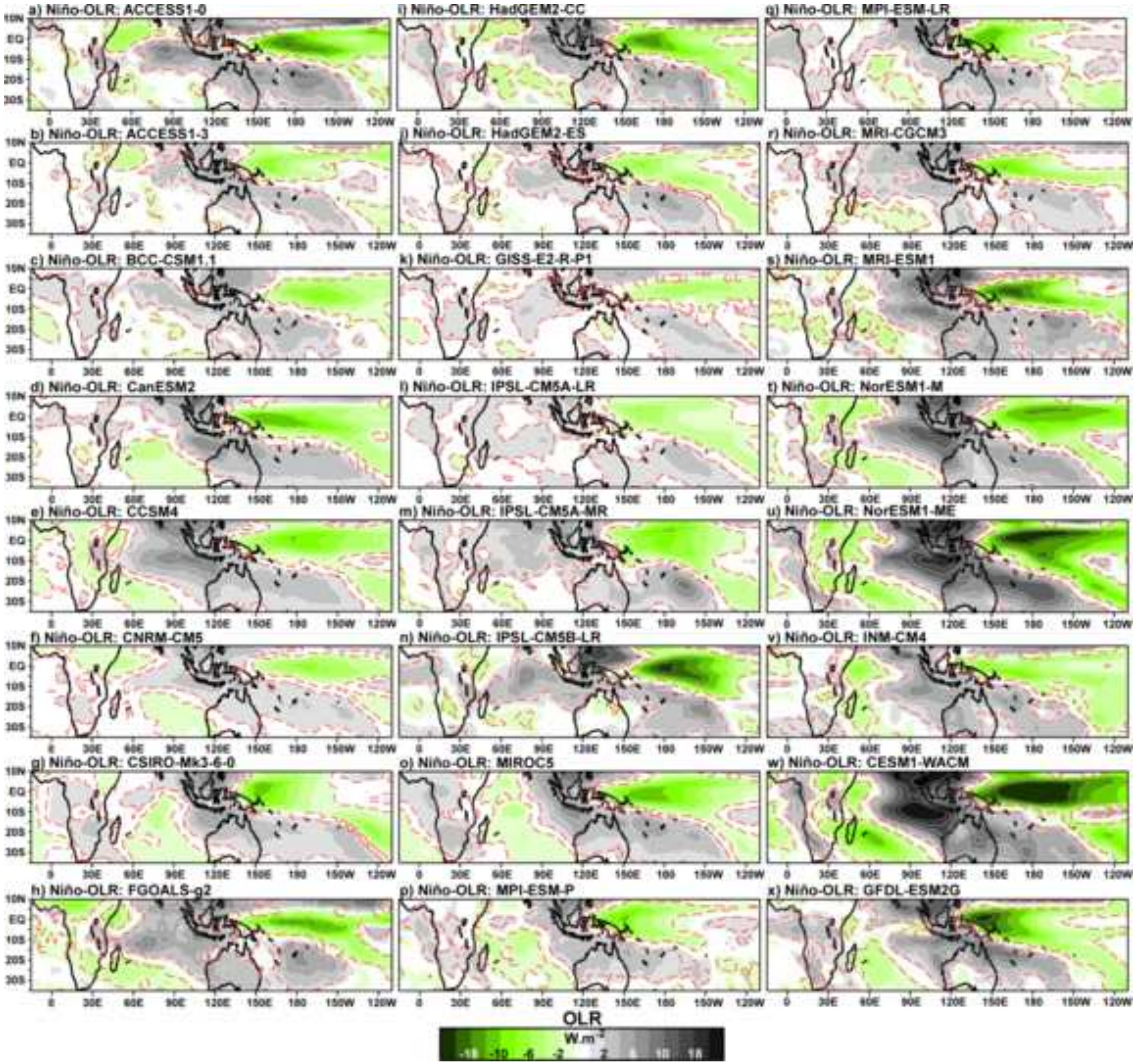

Figure 11
Click here to download high resolution image

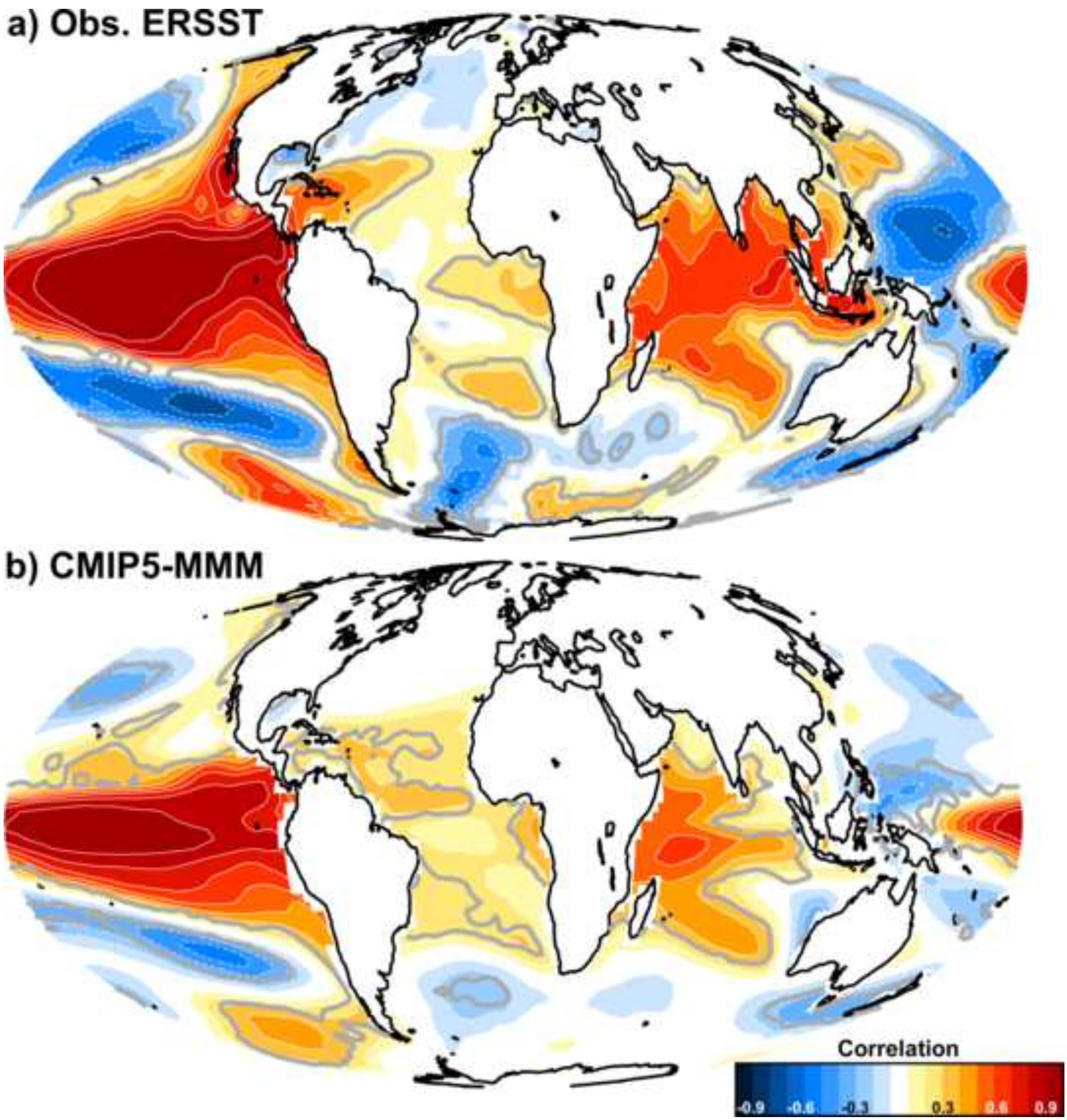

Figure 12

Click here to download high resolution image

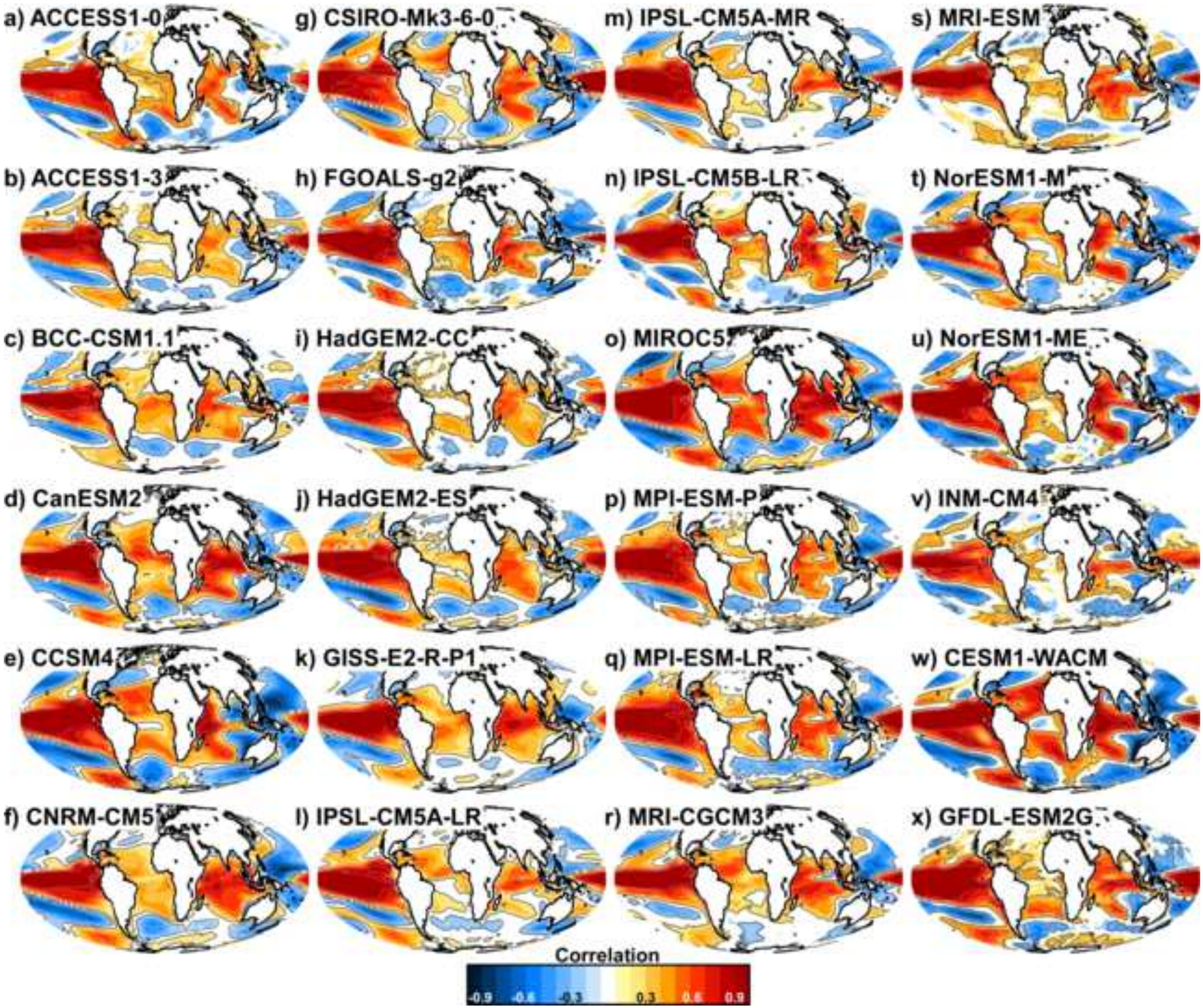

Figure 13

Click here to download high resolution image

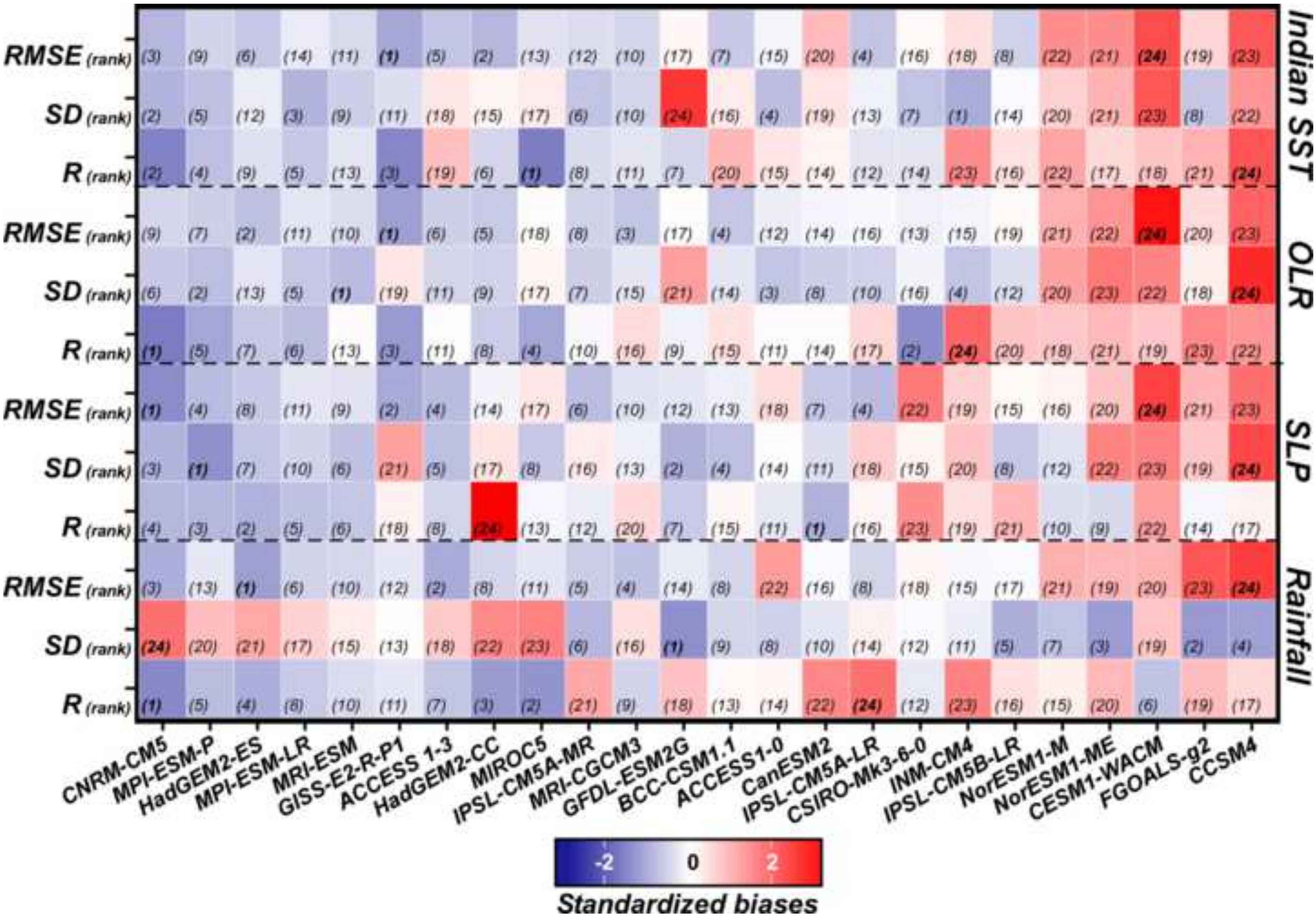

Table 1
Click here to download high resolution image

	Institution	Variables	Name *(ens. member)*	Period
Obs.	CRU, *United Kingdom*	pr	CRU TS 3.21	1950-2005
	NOAA/NCDC, *USA*	sst	ERSST v3b	1950-2005
	NCEP/NCAR, *USA*	slp, U, V, z500, OLR	NCEP-1	1950-2005
CMIP5 models	CSIRO/BOM, *Autralia*	pr, sst, slp, z500, OLR	ACCESS 1.0 *(1)*	1950-2005
	CSIRO/BOM, *Autralia*	pr, sst, slp, z500, OLR	ACCESS 1.3 *(3)*	1950-2005
	BCC, *China*	pr, sst, slp, z500, OLR	BCC-CSM1.1 *(3)*	1950-2005
	CCCma, *Canada*	pr, sst, slp, z500, OLR	CanESM2 *(5)*	1950-2005
	NCAR, *USA*	pr, sst, slp, z500, OLR	CCSM4 *(6)*	1950-2005
	CNRM/CERFACS, *France*	pr, sst, slp, z500, OLR	CNRM-CM5 *(10)*	1950-2005
	CSIRO/QCCCE, *Australia*	pr, sst, slp, z500, OLR	CSIRO-MK3.6.0 *(10)*	1950-2005
	LASG/CESS, *China*	pr, sst, slp, z500, OLR	FGOALS-g2 *(1)*	1950-2005
	MOHC, *United Kingdom*	pr, sst, slp, z500, OLR	HadGEM2-CC *(2)*	1950-2005
	MOHC, *United Kingdom*	pr, sst, slp, z500, OLR	HadGEM2-ES *(4)*	1950-2005
	NASA GISS, *USA*	pr, sst, slp, z500, OLR	GISS-E2-R-P1 *(6)*	1950-2005
	IPSL, *France*	pr, sst, slp, z500, OLR	IPSL-CM5A-LR *(6)*	1950-2005
	IPSL, *France*	pr, sst, slp, z500, OLR	IPSL-CM5A-MR *(3)*	1950-2005
	IPSL, *France*	pr, sst, slp, z500, OLR	IPSL-CM5B-LR *(1)*	1950-2005
	MIROC, *Japan*	pr, sst, slp, z500, OLR	MIROC5 *(5)*	1950-2005
	MPI-M, *Germany*	pr, sst, slp, z500, OLR	MPI-ESM-P *(2)*	1950-2005
	MPI-M, *Germany*	pr, sst, slp, z500, OLR	MPI-ESM-LR *(3)*	1950-2005
	MRI, *Japan*	pr, sst, slp, z500, OLR	MRI-CGCM3 *(3)*	1950-2005
	MRI, *Japan*	pr, sst, slp, z500, OLR	MRI-ESM1 *(1)*	1950-2005
	NCC, *Norway*	pr, sst, slp, z500, OLR	NorESM1-M *(3)*	1950-2005
	NCC, *Norway*	pr, sst, slp, z500, OLR	NorESM1-ME *(1)*	1950-2005
	INM, *Russia*	pr, sst, slp, z500, OLR	INM-CM4 *(1)*	1950-2005
	NSF/DOE/NCAR, *USA*	pr, sst, slp, z500, OLR	CESM1-WACM *(1)*	1950-2005
	NOAA GFDL, *USA*	pr, sst, slp, z500, OLR	GFDL-ESM2G *(1)*	1950-2005